npj | Computational Materials

www.nature.com/npjcompumats

ARTICLE OPEN

Modelling charge transport and electro-optical characteristics of quantum dot light-emitting diodes

Sung-Min Jung[1]✉, Tae Hoon Lee[1], Sang Yun Bang[1], Soo Deok Han[1], Dong-Wook Shin[1], Sanghyo Lee[1], Hyung Woo Choi[1], Yo-Han Suh[1], Xiang-Bing Fan[1], Jeong-Wan Jo[1], Shijie Zhan[1], Jiajie Yang[1], Chatura Samarakoon[1], Yoonwoo Kim[1], Luigi G. Occhipinti[1], Gehan Amaratunga[1] and Jong Min Kim[1]✉

Quantum dot light-emitting diodes (QD-LEDs) are considered as competitive candidate for next-generation displays or lightings. Recent advances in the synthesis of core/shell quantum dots (QDs) and tailoring procedures for achieving their high quantum yield have facilitated the emergence of high-performance QD-LEDs. Meanwhile, the charge-carrier dynamics in QD-LED devices, which constitutes the remaining core research area for further improvement of QD-LEDs, is, however, poorly understood yet. Here, we propose a charge transport model in which the charge-carrier dynamics in QD-LEDs are comprehensively described by computer simulations. The charge-carrier injection is modelled by the carrier-capturing process, while the effect of electric fields at their interfaces is considered. The simulated electro-optical characteristics of QD-LEDs, such as the luminance, current density and external quantum efficiency (EQE) curves with varying voltages, show excellent agreement with experiments. Therefore, our computational method proposed here provides a useful means for designing and optimising high-performance QD-LED devices.

npj Computational Materials (2021)7:122 ; https://doi.org/10.1038/s41524-021-00591-9

Inorganic colloidal quantum dots (QDs) are a class of nanomaterials promising for emissive components of light-emitting diodes (LEDs), owing to their excellent colour saturation, colour tunability, high photoluminescence quantum yield and thermal and electrical stabilities[1–4]. By virtue of the superior properties of QDs as emissive components, the electroluminescence-based quantum-dot light-emitting diodes (QD-LEDs) have emerged as next-generation lighting devices for smart displays and lighting systems with high brightness, low operating voltage and ultimate colour properties[5–7]. Recently, there have been considerable experimental efforts to improve the electro-optical performance of QD-LEDs, and the state-of-the-art QD-LEDs device shows as high as ~20% external quantum efficiency (EQE) for red, green and blue colours with more than 10,000 cd m^{-2} luminance[8–18].

The remarkable achievement of recent QD-LED devices largely relies on the extensive study on QD nanoparticles and the development of property-optimisation procedures via, e.g., engineering core/shell structures and QD surface/ligands[19–22]. The primary aim of the activities was to reduce the source of non-radiative transitions that deteriorates the photoluminescence properties of QDs. The theoretical understanding and experimental methodologies for unravelling non-radiative transition processes for QDs suffice to achieve nearly 100% of photoluminescence quantum yield of QDs[16,23]. Hence, the systematic procedures for developing highly efficient QDs seem to be well established. In contrast, from a device point of view the inspection of individual device components, and its intimate connection to device performance, are relatively much more challenging to be performed experimentally. Consequently, there is a lack of detailed knowledge about device-specific charge-carrier dynamics across QD-LEDs, which is nevertheless essential for characterising and tailoring device performance. Given the complexity of involved physical parameters, therefore, employing a computer simulations appears to be unavoidable.

In fact, many of solid-state LEDs, or organic LEDs, have been developed with the aid of electro-optical simulations based on computational charge transport models[24–28]. The charge transport model for QD-LEDs, however, requires extra consideration of charge-carrier injection and tunnelling processes between a QD and charge transport layer, and between QDs in the emissive layer (EML), respectively: very few such models have been reported to date. A noteworthy charge transport model that has provided a simulation basis for studying QD-LED device was proposed by Kumar et al., and then employed by Vahabsad et al. to simulate the electro-optical properties of QD-LEDs[29–31]. Here, they described, for the first time, charge injections from a transport layer to QD layer in terms of a charge capturing process and charge transport between QDs mediated by a direct interparticle tunnelling process. With their charge transport model, carrier distributions and current densities as a function of bias voltage were analysed by varying physical constants such as Shockley-Read-Hall (SRH) recombination lifetime and radiative recombination strength. However, this model lacks a proper description of charge injection occurring at QD layers: for instance, a consideration of the dependence of capturing coefficient on applied bias voltage was absent, which resulted in inaccurate prediction of threshold voltage. Moreover, in the recombination process of electron–hole pairs, they considered only radiative and SRH non-radiative recombination processes without accounting for the Auger recombination, the dominant non-radiative process at high operational voltages, even though the behaviour of EQE–voltage curve has long been known to critically depend on the Auger recombination process[4,16,18,32–37]. These oversimplifications render the aforementioned model inappropriate for reliably predicting the electro-optical characteristics of QD-LEDs, such as current densities or EQE values as a function of applied voltage.

In this study, we introduce a rigorous charge transport model designed for comprehensively simulating the charge-carrier transport across QD-LED devices, in which the electric-field-

[1]Electrical Engineering Division, Department of Engineering, University of Cambridge, Cambridge, United Kingdom. ✉email: sj569@cam.ac.uk; jmk71@cam.ac.uk

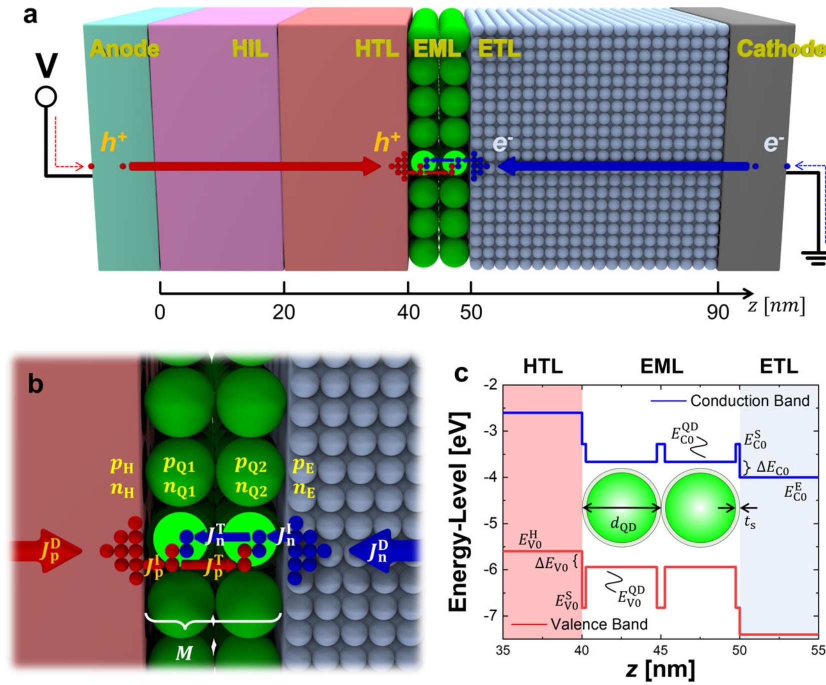

Fig. 1 Device configuration of QD-LED for the charge transport simulation. a Schematic illustration of device architecture. An indium tin oxide (ITO), a poly(3,4-ethylenedioxythiophene)/poly (styrenesulfonate) (PEDOT:PSS), a poly[(9,9-dioctylfluorenyl-2,7-diyl)-co-(4,4′-(N-(4-sec-butylphenyl)diphenylamine)] (TFB), QDs, a zinc oxide (ZnO) and an aluminium (Al) are used for the anode, HIL, HTL, EML, ETL and cathode, respectively. **b** Schematic pathways of possible current flow around the EML. **c** Flat-band energy-level diagram across the QD-LED device. E_{C0}^{QD} and E_{V0}^{QD} are the LUMO and HOMO energy-levels of the QD core, and E_{C0}^{E} and E_{V0}^{H} are the conduction and valance band edges of ETL and HTL, respectively. E_{C0}^{S} and E_{V0}^{S} are the conduction and valance band edges of the QD shell, respectively. d_{QD} and t_s are the diameter of QD particle and the thickness of the QD shell, respectively.

dependent capture process and Auger non-radiative recombination are taken into account. With this simulation model, quantitative information on the distribution of charge carrier densities, electrostatic potentials, as well as radiative and non-radiative recombination rates, could be obtained. The electro-optical characteristics, such as luminance, current densities and EQE curves with varying applied voltages, are also analysed by computer simulations from which the key device parameters for high-performance QD-LEDS are identified. A set of red, green and blue QD-LEDs are fabricated, and their electro-optical characteristics are emulated to validate our charge transport simulation model.

RESULTS

Basic concept of modelling

The device architecture used for the modelling of charge transport in QD-LED is schematically illustrated in Fig. 1a. The device is configured to the conventional stack structure of the hole injection layer (HIL), hole transport layer (HTL), emission layer (EML) and electron transport layer (ETL) sandwiched between anode and cathode electrodes[15]. The EML is treated as a stack of M number of QD layers. As depicted in Fig. 1a, the holes and electrons supplied from a voltage source are transported through the HIL/HTL and ETL, respectively, and are injected into the QD layer. Then, electron–hole pairs are confined to the QD particles, and photons in the visible range are generated by the radiative recombination process of the electron–hole pairs. In order to simulate carrier densities for each QD layer, a single mesh point centred at each QD layer is employed in this study as shown in Fig. 1a. This is because the centre of each QD can be considered as a localised charge-trap site for charge injection from transport layers. Moreover, the charge transport between two QDs can be adequately described by a direct tunnelling process between two charge carriers confined within a potential well of each QD layer[29,30]. These charge transport mechanisms are based on a charge-hopping process, which takes place in materials (such as QDs) where a distance between two localised sites (or particles) is larger than an order of ~1 nm. With this assumption, the charge transports can be calculated with a single mesh point representing a localised state of each QD layer[38,39].

Figure 1b shows the schematic pathways for possible current flow across the QD-LED devices. The charge transports across the device can be described by three types of hole and electron currents: (i) the drift-diffusion current densities J_p^D and J_n^D in the HIL/HTL and ETLs; (ii) tunnelling current densities J_p^T and J_n^T between two neighbouring QD layers, and; (iii) injection current densities J_p^I and J_n^I between the QD layer and charge transport layers. Among the current densities depicted in Fig. 1b, the injection current densities of the majority carriers J_p^I and J_n^I, which are associated with charge capture process between the QD layer and charge transport layers, are described by Eq. (1)[29,40]. Here, the charge injection by minority carriers is neglected under the forward bias condition.

$$
\begin{aligned}
J_p^I &= q r_{QD}\left(\pi r_{QD}^2\right)\sigma_p T_{bp}\mu_{p0}^{QD}\left(F_p^{3/2}/F_0^{1/2}\right)p_H\left(N_{QD}-p_{Q1}\right),\\
J_n^I &= q r_{QD}\left(\pi r_{QD}^2\right)\sigma_n T_{bn}\mu_{n0}^{QD}\left(F_n^{3/2}/F_0^{1/2}\right)n_E\left(N_{QD}-n_{Q2}\right).
\end{aligned}
\tag{1}
$$

Here, q is the electric charge of a proton, and r_{QD} is the radius of QD. πr_{QD}^2 is the cross-sectional area of the QD, and σ_p and σ_n are relative capture cross-sections for the hole and electron, respectively[41–44]. T_{bp} and T_{bn} are hole and electron tunnelling probabilities of the energy-barriers formed by the shell of QDs[45]. μ_{p0}^{QD} and μ_{n0}^{QD} are the hole and electron mobilities of QD layer at an electric field F_0 for Poole–Frenkel law[25]. The conduction and valence energy-levels, (i.e. E_{C0}^{S} and E_{V0}^{S}, respectively) and the thickness, t_s, of the QD shell are considered in our simulation model in order to compute the tunnelling probabilities associated

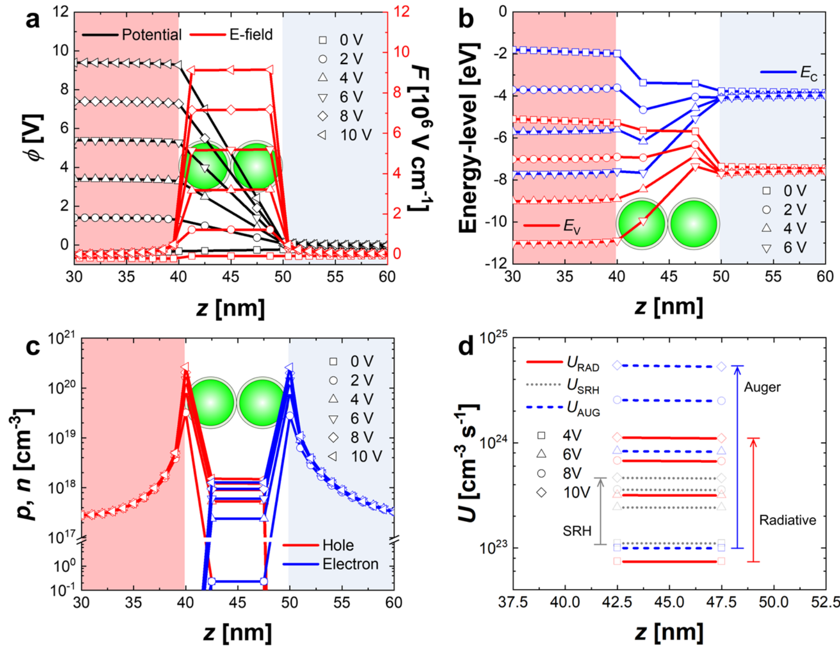

Fig. 2 Internal distributions of physical quantities across the QD-LED device under applied voltages from 0 V to 10 V for every 2 V steps. **a** Potential and electric field distributions. **b** Steady-state energy-level distributions of conduction and valance band around the EML. **c** Distributions of the hole and electron densities around the EML. **d** Radiative, SRH and Auger recombination rates at each QD layers. Here, the number of QD layers M is 2 and the diameter of the QD is 5 nm. The bandgap of the QD core is 2.28 eV for the light wavelength of 545 nm. The LUMO and the HOMO levels of the QD core are −3.66 eV and −5.94 eV so that $\Delta E_{C0} = \Delta E_{V0} = 0.34$ eV, and the charge injection mobilities of hole and electron, α_p and α_n, are both 3.0×10^{-9} cm^2 V^{-1} s^{-1} to balance the holes and electrons accumulated in QD layers.

with the shell of QD layers (Supplementary Methods). F_p and F_n are the electric fields at the HTL/QD and ETL/QD interfaces, respectively, which have been completely neglected in the previous studies[29,30]. p_H and n_E are the hole and electron densities at the HTL and ETL surfaces facing QD layer, respectively, each of which scales with the applied voltage and plays a role of a hole or electron source, respectively, towards an adjacent QD layer. p_{Q1} and n_{Q2} are the hole and the electron densities at the centre of outermost QD layers facing HTL and ETL, respectively. N_{QD} is the density of QDs obtained by the reciprocal of the volume of a single QD particle. In this study, charge-injection mobilities for holes, $\alpha_p = \sigma_p T_{bp} \mu_{p0}^{QD}$, and for electrons, $\alpha_n = \sigma_n T_{bn} \mu_{n0}^{QD}$, are introduced to analyse the effect of the charge injection mismatch on the charge balance in QD layers. With the given current densities defined in each region of the device, the dynamic motion of charge carriers is numerically simulated by solving the continuity equations and Poisson's equation, simultaneously. It should be noted that in the treatment of charge transport processes, as given in Eq. (1), we have dealt with detailed transport processes between QD and charge transport layers of HTL or ETL by taking into account both their electric-field dependence and inter-site distances, which distinguishes, in part, our model from the previous treatment and enables more accurate description of QD-LED devices, as will be shown in the following.

The flat-band energy-level diagram across the device is plotted in Fig. 1c. The valance band offset ΔE_{V0} between HTL and QD core, and the conduction band offset ΔE_{C0} between ETL and QD core, are additionally considered to analyse the effect of charge injection mismatch caused by the difference between the valance and conduction band offsets. The band offsets are defined by $\Delta E_{V0} = E_{V0}^{H} - E_{V0}^{QD}$ and $\Delta E_{C0} = E_{C0}^{QD} - E_{C0}^{E}$. Here, E_{V0}^{QD} and E_{C0}^{QD} are the highest occupied molecular orbital (HOMO) and the lowest unoccupied molecular orbital (LUMO) energy-levels of QD core, and the E_{V0}^{H} and E_{C0}^{E} are the flat band edges of the valance and conduction energy-levels of the HTL and ETL, respectively. Then, the threshold voltage of QD-LED device is theoretically predicted by Eq. (2) with the approximation of linear distribution of a potential field in the EML region.

$$V_{th} \cong \frac{2M}{q} \max(\Delta E_{C0}, \Delta E_{V0}) + V_{bi} \tag{2}$$

Here, V_{bi} is a built-in potential arising from the work-function difference between the cathode and anode electrodes.

Simulation of charge transport in QD-LEDs

Figure 2 shows the internal distributions of various physical quantities around the EML obtained from charge transport simulation under various voltage configurations. A cadmium selenide (CdSe) and a zinc sulphide (ZnS) are used as a core and a shell material of the QD, respectively. All the simulation parameters for QDs and charge transport layers used in the charge transport model are summarised in Supplementary Tables 1 and 2. The electrostatic potentials and their corresponding electric field distributions under the bias voltage ranging from 0 V to 10 V for every 2 V steps were computed based on our model and demonstrated in Fig. 2a. As shown in the figure, the potential linearly decreases only in the EML region, leading to a concentrated electric field in the QD layers. Figure 2b shows the valence and conduction band energy-levels around the EML under different bias conditions. Below 4 V bias voltages, the energy steps, which act as an obstacle to carrier injection, are observed around $z = 40$ nm for holes on the valance-band side and around $z = 50$ nm for electrons on the conduction-band side.

Figure 2c shows the steady-state distribution of carrier densities around the EML under the bias voltage ranging from 0 V to 10 V with every 2 V step. First, the holes and electrons are accumulated at the surfaces of HTL and ETL due to the electric field built between HTL and ETL. Under low bias voltages, the accumulated carriers cannot be injected into the QD layers due to the energy steps caused by band offsets. However, when the bias voltage exceeds 4 V, the energy steps are finally suppressed with the help

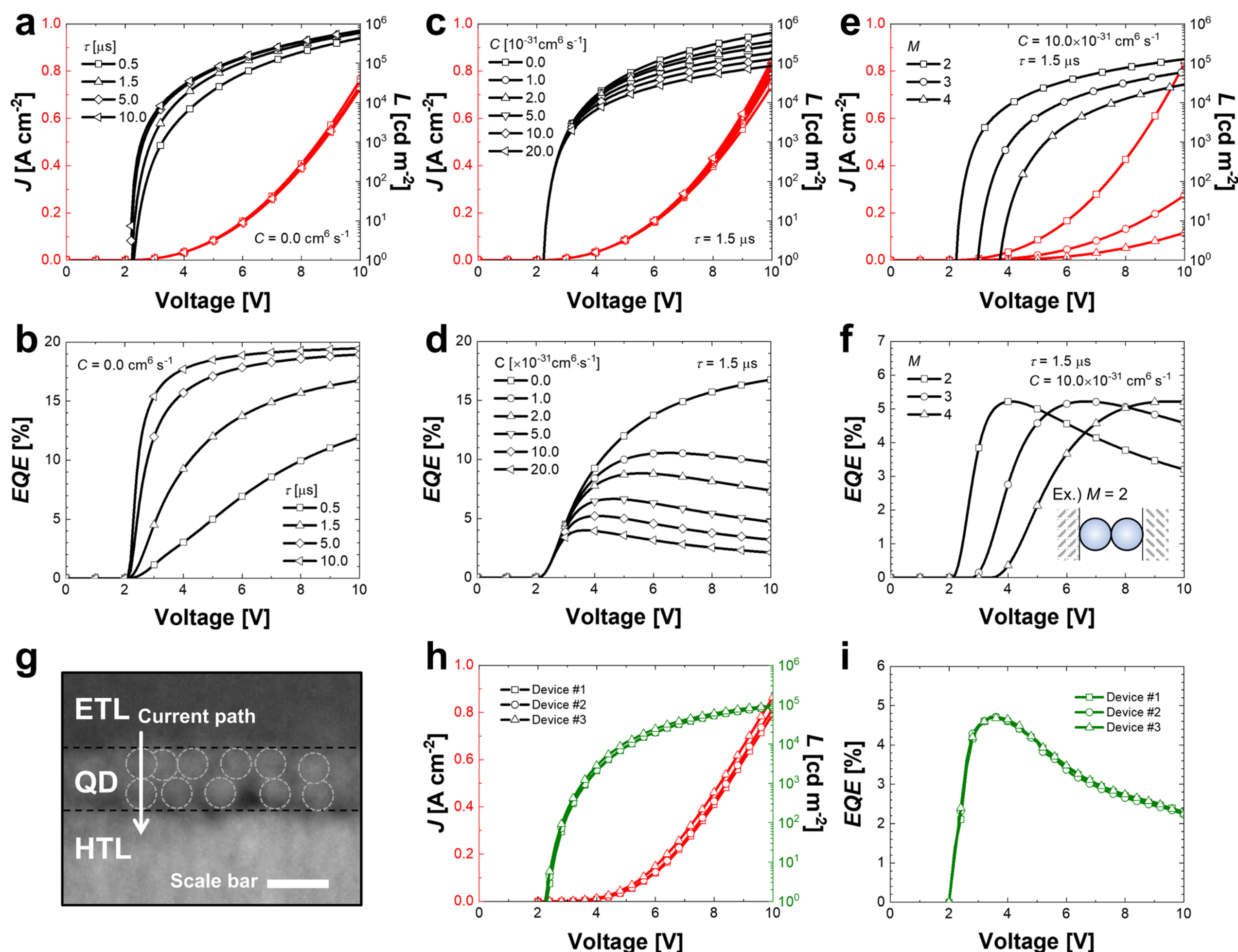

Fig. 3 Variations of the simulated voltage dependences of electro-optical properties of QD-LEDs. Luminance, current density and EQE curves for **a**–**b** different SRH recombination lifetimes, for **c**–**d** different Auger capture probabilities and for **e**–**f** different number of QD layers in EML. *LEE* is considered 20% for the calculation of the EQE curves. **g** TEM image of the cross-section of QD layer. The length of scale bar is 10 nm and the average diameter of QDs is estimated to be around 5 nm. **h**–**i** Luminance, current density and EQE curves obtained experimentally from the green QD-LED samples fabricated in this study. The electro-optical characteristic curves show quite similar behaviours to the simulated results.

of the electrostatic potential and the charges are started to be injected into the QD layers. After the charge injection, carriers move further to the neighbouring QD layer by tunnelling process, and then are blocked by the opposing energy barrier. Hence, the charge carriers are accumulated at each of the QD layers to generate EHPs which are recombined by radiative, SRH and Auger processes. More detailed distribution of physical quantities across the entire device are plotted in Supplementary Figures.

Figure 2d shows the spatial distributions of radiative (U_{RAD}), SRH (U_{SRH}) and Auger (U_{AUG}) recombination rates at each of QD layers within the EML under the applied voltages ranging from 4 V to 10 V. Here, a Langevin recombination strength γ for the radiative recombination rate is calculated to be 0.58×10^{-12} cm^3 s^{-1} in the simulation. For the computation of SRH and Auger recombination rates in QD layers, the hole (τ_p) and electron (τ_n) SRH recombination lifetimes, and the hole (C_p) and electron (C_n) Auger capture probabilities, are assumed to be $\tau_p = \tau_n = \tau = 1.5$ µs and $C_p = C_n = C = 1.0 \times 10^{-30}$ cm^6 s^{-1} (see Methods). At the voltage of 4 V, the SRH recombination process becomes dominant among the various recombination process occurring in the QD layer. However, as the voltage increases from 4 V to 10 V, the Auger recombination rate increases by a factor of 55 when compared with the results at 4 V (9.9×10^{22} cm^{-3} s^{-1}), while the radiative recombination rate becomes 15 times larger than the value at 4 V (7.4×10^{22} cm^{-3} s^{-1}) and the SRH recombination rate increases by a factor of 4 (1.1×10^{23} cm^{-3} s^{-1} at 4 V). Considering that the EQE of device is determined by the ratio of the radiative to the total recombination rate, it is predicted that the EQE of QD-LED decreases with high voltage applications, since the Auger recombination rate increases much faster than the radiative recombination rate.

Recombination processes and electro-optical properties

Figure 3a–f shows the simulated voltage dependencies of the luminance, current density and EQE on the SRH lifetime, Auger capture probability and the number of QD layers. As shown in the figures, all the luminance values on a logarithmic scale increase abruptly just after a certain threshold voltage, while all the current densities on a linear scale monotonically increase. The effects of the SRH lifetime and the Auger capture probability on the electro-optical properties of the QD-LED devices are analysed in Fig. 3a–d. Figure 3a–b shows current densities, luminance and EQE curves simulated with different SRH recombination lifetimes τ ranging from 0.5 µs to 10.0 µs, where the Auger recombination process is neglected ($C = 0$ cm^6 s^{-1}). As shown in Fig. 3a, b, even though the luminance and current density curves are not very sensitive to the variation of the SRH lifetime, the slope of the EQE curve is

significantly affected by the SRH lifetime. When the SRH lifetime is large enough to be over 5.0 µs (i.e. the non-radiative transition due to the SRH recombination becomes very small), the EQE is saturated to an optical light extraction efficiency (LEE) of the device, in the absence of the other non-radiative transition route of Auger recombination process.

Figure 3c–d shows the simulated current density, luminance and EQE curves for Auger capture probabilities C varying from 0 to 20×10^{-31} cm^6 s^{-1}, while fixing the SRH recombination lifetime τ to be 1.5 µs. In Fig. 3c, the luminance decreases significantly while the current density increases slightly, as the Auger capture probability increases. For EQE curves in Fig. 3d, when the Auger capture probability is larger than 1.0×10^{-31} cm^6 s^{-1}, the EQE rolls off once the EQE reaches its maximum value and the EQE drops more severely as the Auger capture probability increases. Therefore, it is found from our charge transport model that the EQE roll-off, which is rather commonly observed in experiments can be largely attributed to the strong activity of Auger recombination process at high bias voltages[9,10,14,15,17,23]. The significance of the Auger process is hence apparent from Fig. 3, thereby rationalising (and necessitating) the inclusion of this recombination process as a main non-radiative transition source in QD-LED charge-transport modelling.

The effects of the number of QD layers, which is another crucial parameter determining device performance, are also analysed by our charge transport model (Fig. 3e, f). The recombination parameters are set to be the same as the parameters used in Fig. 2d. For $M = 2$, the luminance and current density at 10 V are 127,226 cd m^{-2} and 0.83 A cm^{-2}, respectively, and the threshold voltage is obtained to be 2.2 V according to the simulation. As can be predicted from Eq. (2), the threshold voltage rises by around 0.7 V and the luminance decreases by half, as the number of QD layers increases. From the EQE curve for $M = 2$, the maximum EQE is observed to be 5.2% at 4.1 V, and the EQE drops to 3.2% at 10 V due to the Auger recombination process in the QD layer, as illustrated in Fig. 3d. The EQE curves become less steep as the number of QD layers increases, which can be ascribed to the thickness effect on the electric field.

To compare the theoretical predictions with experimental results, three samples of green QD-LED devices were fabricated under the same device condition (Fig. 3g–i). In Fig. 3g, the transmission electronic microscopy (TEM) image shows that about two QD layers are formed between HTL and ETL, corresponding to the assumption of $M = 2$ taken in our simulations. Figure 3h, i shows the experimental current density, luminance and EQE curves for the three green QD-LEDs fabricated in this study. From Fig. 3h, the experimental luminance and current density at 10 V are found to be around 86,000 cd m^{-2} and 0.84 A cm^{-2}, respectively, with the threshold voltage of 2.3 V, whose values turn out to be very similar to the predicted values from our simulation models. In Fig. 3i, the maximum EQE of 4.7% at 3.5 V is observed experimentally and the EQE drops to 2.2% at 10 V from the maximum. It is significant that the shape of luminance, current density and EQE curves obtained from experiment can be described rather quantitively, as described in Fig. 3, indicating that our charge-transport model with selected physical parameters seems to be capable of reproducing most of the essential experimental data necessary for characterising device performance.

Charge balance in QD-LEDs

To gain a comprehensive understanding of the relationship between experimental results and relevant device configurations, the change of the EQE curve under various charge balance conditions is analysed through our simulation models. Figure 4a–c shows the typical shapes of EQE curves (types I, II and III) obtained from various experimental conditions. As illustrated in Fig. 4a–c, the shape of EQE curves strongly depends on device architectures or experimental conditions, and the major factors determining its shape can be quantitatively analysed by our charge transport model. The precise understanding of the relationship between the shape of EQE curves and shape-determining factors is important, as it can indicate a direct qualitative measure of charge imbalance present in device, as will be discussed in detail in the following. Here, the mismatch of charge injection mobilities, α_p and α_n, and the mismatch of the band offsets, ΔE_{C0} and ΔE_{V0}, are examined as major candidate factors determining the charge balance in the QD layers[33].

First, the charge injection is assumed to be perfectly matched, i.e. $\alpha_p = \alpha_n = 3.0 \times 10^{-9}$ cm^2 V^{-1} s^{-1} (α_p:α_n = 1.0:1.0) and $\Delta E_{V0} = \Delta E_{C0} = 0.34$ eV ($\Delta E_{V0} - \Delta E_{C0} = 0$ eV), as shown in Fig. 4d–f. Here, the number of QD layer M is assumed to be 3. For the charge-balanced condition (Fig. 4d), the hole and electron densities at QD become similar to each other as the voltage increases. The slight difference between hole and electron densities is caused by the difference in the dielectric constants of ETL and HTL, and by other minor material properties. As the voltage increases, SRH, radiative and Auger recombination rates are activated in the order shown in Fig. 4e, but the Auger recombination rate overtakes the other recombination rates after 6.7 V bias voltage. Therefore, in the charge-balanced condition, the voltage at the maximum EQE is obtained to be 6.7 V (Fig. 4f) and the EQE drops slowly after the voltage at the maximum EQE. Here, the threshold voltage is observed to be 2.9 V in the charge-balanced condition.

However, when the charge injection is unbalanced (Fig. 4g–i) by the difference in the charge injection mobilities, that is, $\alpha_p \neq \alpha_n$ (α_p:α_n = 0.5:1.5 for electron-rich and 1.5:0.5 for hole-rich conditions) with $\Delta E_{V0} = \Delta E_{C0}$, the majority carrier density is 100 times larger than the minority carrier density (Fig. 4g). In Fig. 4h, due to the large charge density difference, the Auger recombination rate overtakes the other recombination rates at 4 V, which is lower than the voltage at the maximum EQE in the charge-balanced condition (Fig. 4e). Hence, the EQE quickly reaches the maximum at 4 V and drops rapidly as the voltage further increases, resulting in a steeper curve compared to the case of the charge-balanced condition (Fig. 4i).

On the other hand, when the charge injection is unbalanced (Fig. 4j–l) by the difference in the band offsets, that is, $\Delta E_{V0} \neq \Delta E_{C0}$ ($\Delta E_{V0} - \Delta E_{C0} = -0.4$ eV for hole-rich and $\Delta E_{V0} - \Delta E_{C0} = +0.4$ eV for electron-rich cases), while the charge injection mobilities are the same ($\alpha_p = \alpha_n$), the difference between the hole and electron densities become more significant (Fig. 4j). This is because charge carriers crossing a smaller band offset can be more easily injected into the QD layer than the carriers crossing a larger band offset. The threshold voltage is measured to be 4.1 V, which is 1.2 V larger than that for the charge-balanced condition ($V_{th} = 2.9$ V in Fig. 4d–f) due to the difference in the band offsets. Owing to the extremely large carrier density at the threshold voltage, the Auger recombination overtakes the other recombination rate just after the threshold voltage (Fig. 4k). Consequently, the EQE is peaked near the threshold voltage and abruptly decreases with further increase in bias voltage, as plotted with black lines in Fig. 4l. In this simulation condition, since the radiative recombination rate increases slightly faster than the Auger recombination rate at high voltage range, the EQE also increases slightly in this high voltage range. The EQE curves for more complicated unbalanced-charge injection conditions, where $\alpha_p \neq \alpha_n$ and at the same time $\Delta E_{V0} \neq \Delta E_{C0}$, are also plotted in Fig. 4l. When the charge injection is extremely unbalanced, the EQE keeps decreasing after reaching its maximum value, resulting in a EQE curve similar to the type III (Fig. 4c).

Charge transport model and experimental results

To emulate experimentally measured electro-optical characteristics of QD-LEDs via our charge transport simulations, we fabricated

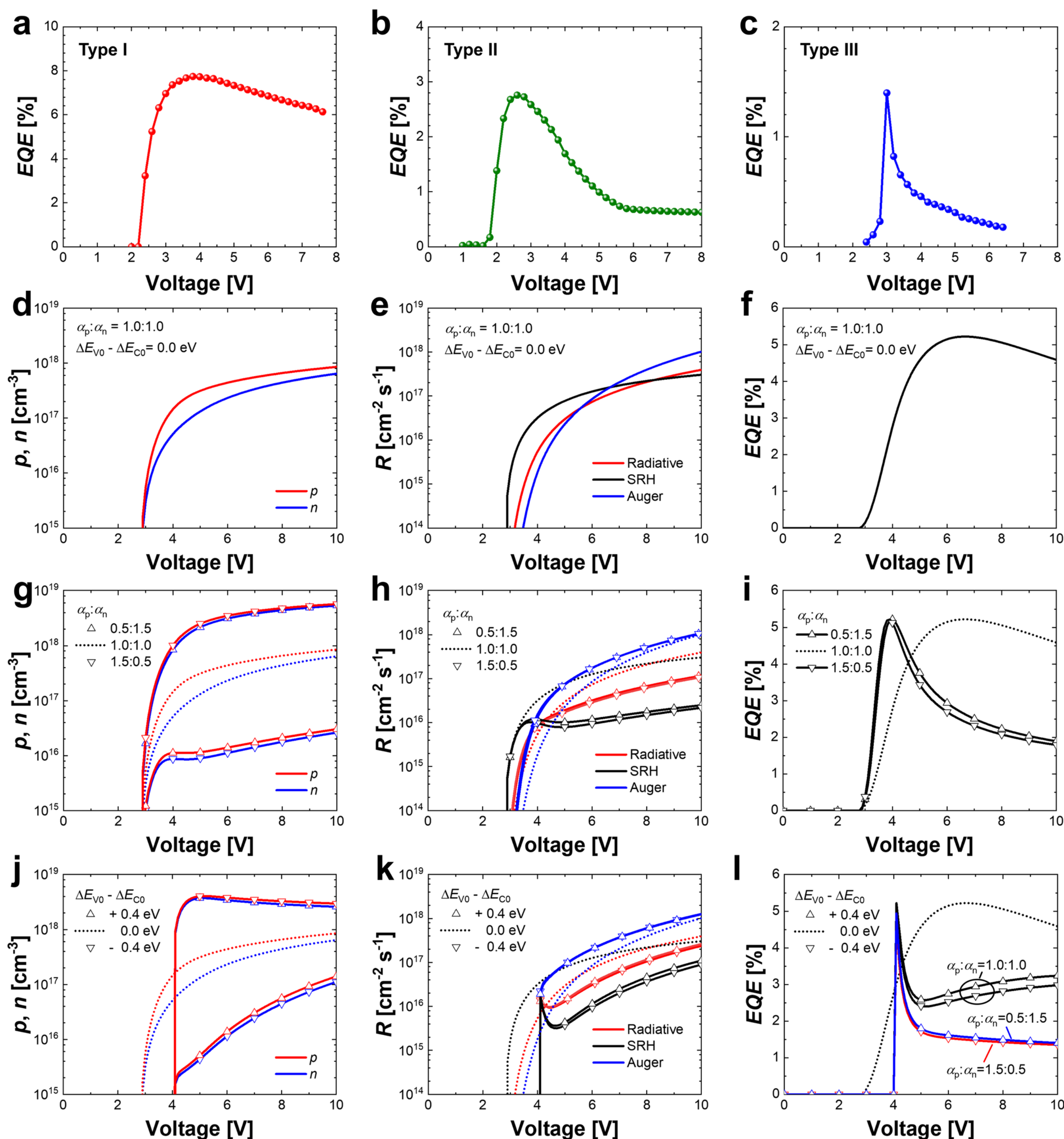

Fig. 4 Changes of the EQE curve according to the various charge balance conditions. a–c Typical EQE curves obtained by experiments for the various device and process conditions. Voltage dependences of **d** hole and electron densities, **e** radiative, SRH and Auger recombination rates and **f** EQE curves for the charge-balanced condition that $\alpha_p = \alpha_n$ with $\Delta E_{V0} = \Delta E_{C0}$. Voltage dependences of **g** hole and electron densities, **h** radiative, SRH and Auger recombination rates and **i** EQE curves for the condition that $\alpha_p \neq \alpha_n$ (α_p:α_n = 0.5:1.5 for electron-rich and 1.5:0.5 for hole-rich conditions) with $\Delta E_{V0} = \Delta E_{C0}$. Voltage dependences of **j** hole and electron densities, **k** radiative, SRH and Auger recombination rates and **l** EQE curves for the condition that $\Delta E_{V0} \neq \Delta E_{C0}$ ($\Delta E_{V0} - \Delta E_{C0} = +0.4$ eV for electron-rich and $\Delta E_{V0} - \Delta E_{C0} = -0.4$ eV for hole-rich conditions).

a set of red, green and blue QD-LED devices. The electro-optical characteristics of the QD-LEDs obtained from the experiments are plotted in Fig. 5a, b. The inset in Fig. 5a shows the snapshots of the fabricated red, green and blue QD-LEDs. The CdSe/ZnS core/shell red and green QDs with their diameters of 7 nm and 5 nm, respectively, are used for red and green QD-LED devices[46], and cadmium zinc sulphide (CdZnS)/ZnS QDs with its diameter of 10.8 nm is used for the blue QD-LED devices. From Fig. 5a, the luminance values of red, green and blue QD-LED devices are measured to be 31,230 cd m^{-2} at 6.0 V, 79,520 cd m^{-2} at 7.6 V and 1423 cd m^{-2} at 8.0 V, respectively, while their threshold voltages are observed to be 1.8, 2.2 and 4.0 V, respectively. The maximum EQEs are found to be 10.5% at 4.0 V, 7.7% at 3.8 V and 1.6% at 5.4 V, respectively, and their EQEs slightly drop to 10.0% at 6.0 V, 6.5% at 7.6 V and 1.2% at 8.0 V for the respective devices (Fig. 5b).

Figure 5c, d shows the luminance, current density and EQE curves emulated by our charge transport simulation model with adjusted material and device parameters. The simulation

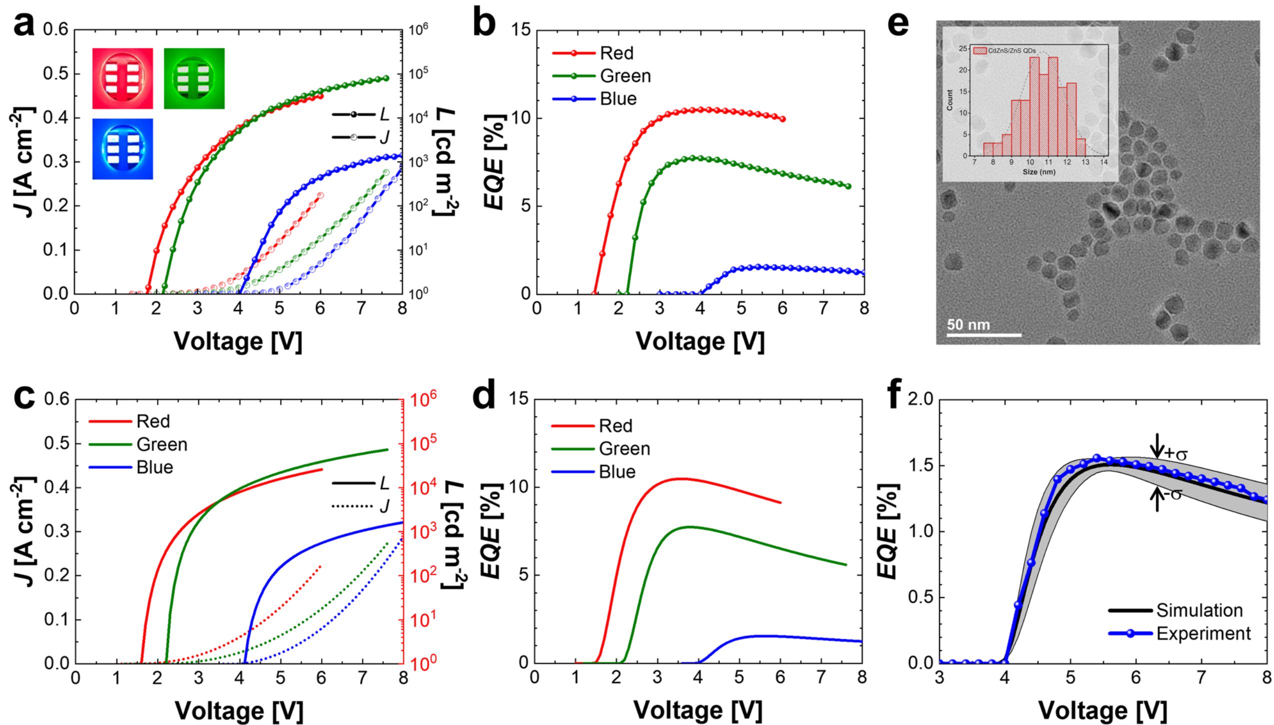

Fig. 5 Comparisons of the simulated and experimental electro-optical characteristics of red, green and blue QD-LED devices. Based on the same device architecture, red (628 nm), green (545 nm) and blue (465 nm) QDs having the optical bandgaps of 1.97, 2.28 and 2.67 eV are used for the simulation, respectively. **a** Luminance and current density curves and **b** EQE curves measured from the fabricated red, green and blue QD-LEDs. Insets are snapshots of the fabricated red, green and blue QD-LED devices. **c** Luminance and current density curves and **d** EQE curves of the red, green and blue QD-LED devices emulated by the charge transport simulation model. **e** TEM image of the blue QDs. Inset is the histogram of the blue QD particle size. **f** Variation of simulated EQE curves within the standard deviation (σ) range for the measured particle size distribution.

Table 1. Parameters for the charge transport simulation to emulate the experimental curves of red, green and blue QD-LED devices fabricated in this study.

Simulation parameters of QDs	Device		
	Red ($\lambda_0 = 628$ nm)	Green ($\lambda_0 = 545$ nm)	Blue ($\lambda_0 = 465$ nm)
Materials (core/shell)	CdSe/ZnS	CdSe/ZnS	CdZnS/ZnS
LUMO [eV]	−3.82	−3.66	−3.47
Bandgap, E_G^{QD} [eV]	1.97	2.28	2.67
Diameter [nm]	7.0	5.0	10.8
Number of QD layer, M	2	2	3
SRH time constant, $\tau_p = \tau_n$ [μs]	4.0	3.0	1.1
Auger probability, $C_p = C_n$ [cm^6 s^{-1}]	2.8×10^{-31}	6.3×10^{-31}	130.0×10^{-31}
Charge injection mobility, $\alpha_p = \alpha_n$ [cm^2 V^{-1} s^{-1}]	1.15×10^{-8}	2.26×10^{-9}	1.45×10^{-7}

parameters for each of the fabricated red, green and blue QD-LEDs are summarised in Table 1. The simulated luminance curves for red, green and blue QD-LED devices (Fig. 5c) exhibit the luminance values of 25,867 cd m^{-2} at 6.0 V, 72,905 cd m^{-2} at 7.6 V and 1633 cd m^{-2} at 8.0 V, respectively, with the threshold voltages of 1.6, 2.2 and 4.1 V for each device. The maximum EQE values (Fig. 5d) are found to be 10.5% at 3.6 V, 7.7% at 3.8 V and 1.5% at 5.6 V, and the EQEs drop to 9.1% at 6 V, 5.6% at 7.6 V and 1.2% at 8.0 V for the red, green and blue QD-LED devices, respectively. As shown in the figures, for all the QD-LED devices the simulated EQE, luminance and current density curves coincide very well with the experimental results, and their quantitative values are also comparable to the experimental results.

Finally, the deviation of EQE curves with respect to QD size distributions is analysed statistically by our charge transport model. The particle size of CdZnS/ZnS core/shell QDs for blue QD-LED device was measured by TEM (Fig. 5e). The average particle size is found to be 10.8 nm, ranging from 7.5 nm to 13.0 nm (the inset in Fig. 5e). For all the measured sizes of QD particles, the EQE curves are simulated, and the variation of EQE curves within the standard deviation (σ) range is plotted in Fig. 5f as a grey-coloured area. Also, the simulated EQE curve (black) averaged over the varying sizes of QDs and the experimental EQE curve (blue) are compared in Fig. 5f. The experimental one resides within $\pm\sigma$ range of the simulated EQE variation. Considering that the experimental EQE curve comes from an ensemble of QDs with varying sizes, the data in Fig. 5f indicates that our charge transport model seems to

be able to take the effect of QD size distributions into account in QD-LED device modelling, which may become important, in particular, for the case where the size distribution of QD is broad.

From Fig. 5, it is clearly noticed that the luminance, current densities and EQE curves obtained from our charge transport model nicely emulate the underlying features of experimental curves, including the presence of threshold voltage and the emergence of a peak in EQE curves. As already emphasised in the previous sections, the central aspects of the current charge transport model, enabling accurate description of electro-optical properties, amounts to the comprehensive treatment of charge transport processes between almost all the device components, and of the radiative and non-radiative transition processes occurring at emitting QD layers. The important parameters determining, for instance, the EQE curves, identified from a comparison with experimentally measured EQE curves, are the SRH and Auger recombination processes that constitute the major non-radiative transition routes. The shape of EQE curve then depends differently on the strength of applied bias voltages: at voltages slightly higher than a threshold voltage, the SRH recombination process plays an important role, but at higher voltages the Auger non-radiative recombination route becomes dominant. As a result of the latter process, which takes place in common for every device, EQE curves show a maximum at a peak voltage, which is device-dependent, and then diminish for the voltage higher than the peak voltage. The maximum EQE value at a peak voltage naturally relies on the balance between the SRH and Auger recombination rates. The difference in conduction or valence energy levels of constituting device materials (notably, QD, ETL and HTL), along with associated contrast in charge-carrier injection mobilities, also significantly affects the EQE curve, both of which might be comprehensively discussed in terms of charge imbalance present in the EML of devices. The impacts of the device or material parameters on the other electro-optical properties, such as current densities or luminescence spectra, could be also revealed within our simulation framework. Hence, the current study demonstrates the potential that both materials and device architectures of QD-LEDs can be designed and optimised by computer simulations based on the charge transport model proposed in this study.

DISCUSSION

In this study, a device simulation model that describes the charge-carrier transport across a QD-LED has been demonstrated. With this model, various electro-optical properties of QD-LEDs were thoroughly analysed by performing computer simulations with varied material and device parameters. The charge-carrier injections from the transport layer to the QD layer are described by the carrier-capturing process of the QDs, together with the consideration of the band offsets between the transport and QD layers. The voltage-dependant electro-optical characteristic curves, such as luminance, current density and EQE curves, were analysed by varying SRH recombination lifetime, Auger capture probability and the number of QD layers in the emissive layer. From the simulation, it was numerically found that the maximum EQE values and the roll-off of the EQE are strongly affected by the SRH recombination lifetime and Auger capture probability. The threshold voltage of QD-LEDs is, on the other hand, determined by the number of QD layers and the difference of band offsets between QD and transport layers. The effects of charge balance conditions were also analysed by the charge transport model, and typical types of EQE curves for various experimental conditions were clearly explained by the simulation in terms of the charge balances.

To validate our simulation model through the comparison with experimental results, red, green and blue QD-LED devices were fabricated via solution process. The comparison reveals that our simulation model is capable of reproducing all the characteristic features of experimental data, including the shape of the graph. Considering the excellent agreement with computational results and experimental data, our proposed charge transport model may provide a useful pathway for understanding, optimising or even designing materials and device architectures for high-performance QD-LEDs by computer simulations.

METHODS

Charge transport model of QD-LEDs

Assuming that all the layers are stacked along the *z*-axis and all the variables are invariant to *x*- and *y*-axes in Cartesian coordinate system, carrier transport within the device at a given time *t* can be described by the following set of time-dependent continuity equations for the hole and electron densities, $p(z, t)$ and $n(z, t)$.

$$\frac{\partial p}{\partial t} = -\frac{1}{q}\frac{\partial J_p}{\partial z} - U, \qquad \frac{\partial n}{\partial t} = \frac{1}{q}\frac{\partial J_n}{\partial z} - U. \tag{3}$$

Here, J_p and J_n are the current densities of the hole and electron, and U is a recombination rate of the carriers, respectively. Among the current densities depicted in Fig. 1b, the drift-diffusion current densities of the hole and electron, J_p^D and J_n^D, are described by the sum of the drift and diffusion current densities as expressed in Eq. (4)[28].

$$J_p^D = q\mu_p p F_p - \mu_p k_B T\frac{\partial p}{\partial z}, \qquad J_n^D = q\mu_n n F_n + \mu_n k_B T\frac{\partial n}{\partial z}. \tag{4}$$

Here, μ_p and μ_n are the hole and electron mobilities in the given semiconductors, F_p and F_n are electric fields acting on the hole and electron. The electric fields are obtained from the gradients of the energy distributions of conduction and valence bands in conjunction with the potential distribution induced by the voltage applied to the QD-LEDs. k_B is the Boltzmann constant and T is the absolute temperature of the device. The tunnelling current densities of the hole and electron, depicted in Fig. 1b, are described by the carrier exchanges from tunnelling process between two adjacent QDs as described in Eq. (5)[29].

$$J_p^T = -q\nu_p d_{QD}(p_{m+1} - p_m), \qquad J_n^T = q\nu_n d_{QD}(n_{m+1} - n_m) \tag{5}$$

Here, ν_p and ν_n are tunnelling frequencies of the hole and electron oscillating between two QDs (Supplementary Methods). d_{QD} is the diameter of QD, and p_{m+1}, p_m, n_{m+1} and n_m are the hole and electron densities at the QD layer indexed with m and m+1.

In Eqs. (1) and (4), the electric field intensity F_p and F_n can be calculated by the derivatives of conduction and valence energy-levels, such that $F_p = (1/q)\partial E_C(z)/\partial z$ and $F_n = (1/q)\partial E_V(z)/\partial z$, where the $E_C(z) = E_{C0}(z) - q\varphi(z)$ and $E_V(z) = E_{V0}(z) - q\varphi(z)$, respectively, from the electrostatic potential $\varphi(z)$ across the device. $E_{C0}(z)$ and $E_{V0}(z)$ are the flat-band energy-level distributions of conduction and valence bands which are plotted in Fig. 1c. The electrostatic potential $\varphi(z)$ is solved by the following Poisson's equation[28].

$$\varepsilon_0\frac{\partial}{\partial z}\left(\varepsilon_r\frac{\partial\varphi}{\partial z}\right) = -q\left(p - n + N_d^+ - N_a^-\right) \tag{6}$$

Here, ε_0 and ε_r are the permittivity of free space and the dielectric constant of a given material, respectively. N_d^+ and N_a^- are the donor and acceptor doping densities of semiconductor layers, respectively.

The recombination rate U in Eq. (3) is defined by the sum of SRH recombination rate U_{SRH}, Auger recombination rate U_{AUG} and radiative recombination rate U_{RAD}[28,29,34,35,47]. As non-radiative recombination rates, the SRH and Auger recombination rates are expressed as the following equations.

$$U_{SRH} = \frac{pn - n_i^2}{\tau_n(p + n_i) + \tau_p(n + n_i)} \tag{7}$$

$$U_{AUG} = \left(C_p p + C_n n\right)\left(pn - n_i^2\right) \tag{8}$$

Here, n_i is an intrinsic carrier density of the given material. τ_p and τ_n are the hole and electron SRH recombination lifetimes, and C_p and C_n are the hole and electron Auger capture probabilities, respectively[36,37,48]. The radiative recombination is only valid within the EML region and expressed as the

following equation.

$$U_{RAD} = \gamma(pn - n_i^2) \tag{9}$$

Here, γ is the Langevin recombination strength which is calculated from $\gamma = q(\mu_{p0}^{QD} + \mu_{n0}^{QD})/(\varepsilon_r^{QD}\varepsilon_0)$ with the hole and electron mobilities and the permittivity of QD layer[47,49].

Boundary conditions

As boundary conditions of the continuity equation, Dirichlet boundary condition is used to describe the carrier densities on the metal contacts of the semiconductor. The hole and electron densities at the metal contact surface of the semiconductor, p_s, n_s are described by Eq. (10).

$$\begin{aligned} p_s &= n_{i,s}\exp\{[\phi_m - (\chi + E_G/2)]/(k_B T)\} \\ n_s &= n_{i,s}\exp\{-[\phi_m - (\chi + E_G/2)]/(k_B T)\} \end{aligned} \tag{10}$$

Here, $n_{i,s}$ is the intrinsic carrier density of the semiconductor, where s denotes the boundary surface of metal contact. ϕ_m is the work-function of the metal electrode, χ and E_G are the electron affinity and the energy bandgap of the given semiconductor. Once the boundary conditions of the hole and electron densities for the continuity equations are determined, the Dirichlet boundary condition is also used for solving the potential distribution function from the Poisson's equation in Eq. (6). Assuming the cathode is connected to the ground, the potential value at the surface interfacing the anode electrode is determined to $V_{appl} - V_{bi}$ with the applied voltage V_{appl} and the built-in potential V_{bi}. The built-in potential is given by $V_{bi} = (\phi_{m,a} - \phi_{m,c})/q$ for the work-functions of the anode and cathode metals, $\phi_{m,a}$, $\phi_{m,c}$, respectively.

Optimal LUMO level of QD

In order to minimise the threshold voltage of the QD-LED device, along with satisfying the charge balance between the hole and electron, the band offsets between QD and charge transport layers need to be the same ($\Delta E_{V0} = \Delta E_{C0}$), according to Eq. (2). The optimal LUMO level of QD core for the charge-balanced condition can be obtained by the following equation.

$$E_{C0}^{QD} = \frac{1}{2}\left(E_{V0}^{H} + E_{C0}^{E}\right) + \frac{1}{2}E_G^{QD} \tag{11}$$

Here, E_G^{QD} is the optical bandgap of QD core, and E_{V0}^{H} and E_{C0}^{E} are aforementioned valance band edge of HTL and conduction band edge of ETL, respectively.

Material and device parameters

The thicknesses of the HIL, HTL and ETL are considered to have 20, 20 and 40 nm, respectively. The dielectric constants ε_r of HIL, HTL and ETL for the computation of the potential distribution are 3.0, 3.5 and 8.5, respectively. The hole and electron mobilities of QD, μ_{p0}^{QD} and μ_{n0}^{QD}, are assumed to be $1.0 \times 10^{-6}\ cm^2\ V^{-1}\ s^{-1}$ and $2.0 \times 10^{-6}\ cm^2\ V^{-1}\ s^{-1}$, respectively. The Langevin recombination strength is calculated to be $0.58 \times 10^{-12}\ cm^3\ s^{-1}$ in the simulation[47]. The diameter of green and red CdSe/ZnS QD are assumped to be 5 and 7 nm, respectively[46]. The thickness of the ZnS shell is also assumped to be 0.5 nm. The energy-levels of conduction and valence bands for the ZnS shell are −3.28 and −6.82 eV, respectively[50]. The built-in potential V_{bi} is 0.64 V from the work-function difference between anode and cathode electrodes. The dielectric constants[51–53], carrier mobilities[51,54,55], doping conditions[29,31,56], electron affinities and work-functions[31,57–59] of the anode electrode, HIL, HTL, ETL and cathode electrode were appropriately chosen from the references. All the simulation parameters for QDs and charge transport layers used in the charge transport model are summarised in Supplementary Tables.

Characterisation of electro-optical properties

The EQE representing the electro-optical properties is calculated by the ratio of radiative recombination rate, R_{RAD}, out of total recombination rate over the entire QD-LED, R_{TOT}, as expressed in Eq. (12) with *LEE* of the given QD-LED device.

$$EQE = LEE \times \frac{R_{RAD}}{R_{TOT}} = LEE \times \frac{\int U_{RAD}\,dz}{\int U_{RAD} + U_{SRH} + U_{AUG}\,dz} \tag{12}$$

Here, the *LEE* was assumed to be 20% in the simulation. The total radiative recombination rate R_{RAD} and total recombination rate R_{TOT} are calculated by integrating U_{RAD} over the EML region and by integrating $U = U_{RAD} + U_{SRH} + U_{AUG}$ over the entire region of the device. The luminance of the electroluminescence-based QD-LEDs are directly calculated from the total radiative recombination rate R_{RAD}. Assuming that the emitted light has the forms of Gaussian distribution for wavelength and Lambertian distribution for polar emission angle, the spectral radiance $L_e(\lambda)$ is expressed as the following equation.

$$L_e(\lambda) = LEE \times \frac{E_G^{QD} R_{RAD}}{\pi^{3/2}}\frac{2\sqrt{\ln 2}}{FWHM}\exp\left[-\frac{4\ln 2}{FWHM^2}(\lambda - \lambda_0)^2\right] \tag{13}$$

The distribution of the spectral radiance is derived from the assumption which the integral of the spectral radiance by the wavelength and solid angle over the visible range and hemisphere equals to the total optical power of light emitted from the QD-LED device. E_G^{QD} is the optical bandgap of QD, λ and λ_0 are the wavelength of emitted light and the peak wavelength of the given QD, respectively. Then, the luminance of the QD-LED device L_v is obtained from the following Eq. (14) for the photopic luminosity function $\bar{y}(\lambda)$.

$$L_v = 683.002(lm/W)\int_{380}^{780}\bar{y}(\lambda)L_e(\lambda)d\lambda \tag{14}$$

Fabrication of QD-LED

In order to compare the simulation results with experiments, red, green and blue QD-LEDs are fabricated by the solution process with the hexane-based colloidal QD solution of 12.5 mg ml^{-1} concentration. The CdSe/ZnS red and green QDs are purchased from Xingshuo Nanotech Co., Ltd., and the CdZnS/ZnS blue QDs are synthesised in the laboratory[32]. The solution phase of PEDOT:PSS (Al 4083), TFB (8 mg ml^{-1} in chlorobenzene), magnesium-doped ZnO (70 mg ml^{-1} in butanol) are used for the materials of HIL, HTL and ETL, respectively. After cleaning the patterned ITO glass substrate, PEDOT:PSS layer is spin-coated at 3000 revolution per minute (rpm) spin-speed and annealed at 150 °C on the hot plate for 30 min. Subsequently, TFB precursor is spin-coated at 3000 rpm spin-speed and annealed at 130 °C on the hot plate for 30 min. The QD and ZnO layers are sequentially formed on the TFB layer by spin-casting under each spin-speed of 3000 and 4000 rpms and annealed at 110 °C on the hot plate for 15 min, respectively. Finally, the aluminium layer is deposited on the ZnO surface to form a cathode electrode by a thermal evaporation process.

DATA AVAILABILITY

The data that support the plots within this paper and other findings of this study are available from the corresponding authors upon reasonable request.

CODE AVAILABILITY

The codes developed in this study are available from the authors upon reasonable request.

Received: 7 April 2021; Accepted: 13 July 2021;
Published online: 29 July 2021

REFERENCES

1. Ekimov, A. I. & Onushchenko, A. A. Quantum size effect in three-dimensional microscopic semiconductor crystals. *JETP Lett.* **34**, 345–348 (1981).
2. Cho, K.-S. et al. High-performance crosslinked colloidal quantum-dot light-emitting diodes. *Nat. Photonics* **3**, 341–345 (2009).
3. Dai, X. et al. Solution-processed, high-performance light-emitting diodes based on quantum dots. *Nature* **515**, 96–99 (2014).
4. Lee, T. et al. Highly efficient and bright inverted top-emitting InP quantum dot light-emitting diodes introducing a hole-suppressing interlayer. *Small* **15**, 1905162 (2019).
5. Colvin, V. L., Schlamp, M. C. & Allvlsatos, A. P. Light-emitting diodes made from cadmium selenide nanocrystals and a semiconducting polymer. *Nature* **370**, 354–356 (1994).
6. Kathirgamanathan, P., Bushby, L. M., Kumaraverl, M., Ravichandran, S. & Surendrakumar, S. Electroluminescent organic and quantum dot LEDs: the state of the art. *J. Disp. Technol.* **11**, 480–493 (2015).
7. Choi, M. K., Yang, J., Hyeon, T. & Kim, D.-H. Flexible quantum dot light-emitting diodes for next-generation displays. *NPJ Flex. Electron* **2**, 1–14 (2018).

8. Bae, W. K. et al. Multicolored light-emitting diodes based on all-quantum-dot multilayer films using layer-by-layer assembly method. *Nano Lett.* **10**, 2368–2373 (2010).
9. Qian, L., Zheng, Y., Xue, J. & Holloway, P. H. Stable and efficient quantum-dot light-emitting diodes based on solution-processed multilayer structures. *Nat. Photonics* **5**, 543–548 (2011).
10. Kim, T.-H. et al. Full-colour quantum dot displays fabricated by transfer printing. *Nat. Photonics* **5**, 176–182 (2011).
11. Kim, T.-H. et al. Heterogeneous stacking of nanodot monolayers by dry pick-and-place transfer and its applications in quantum dot light-emitting diodes. *Nat. Commun.* **4**, 1–9 (2013).
12. Vasan, R., Salman, H. & Manasreh, M. O. All inorganic quantum dot light emitting devices with solution processed metal oxide transport layers. *MRS Adv.* **1**, 305–310 (2016).
13. Jesuraj, P. J. et al. Effects of doping concentration and emission layer thickness on recombination zone and exciton density control in blue phosphorescent organic light-emitting diodes. *ECS J. Solid State Sc.* **6**, R170–R174 (2017).
14. Zhang, H., Chen, S. & Sun, X. W. Efficient red/green/blue tandem quantum-dot light-emitting diodes with external quantum efficiency exceeding 21%. *ACS Nano* **12**, 697–704 (2018).
15. Shen, H. et al. Visible quantum dot light-emitting diodes with simultaneous high brightness and efficiency. *Nat. Photonics* **13**, 192–197 (2019).
16. Won, Y. H. et al. Highly efficient and stable InP/ZnSe/ZnS quantum dot light-emitting diodes. *Nature* **575**, 634–638 (2019).
17. Zhang, H., Su, Q. & Chen, S. Suppressing Förster resonance energy transfer in close-packed quantum-dot thin film: Toward efficient quantum-dot light-emitting diodes with external quantum efficiency over 21.6%. *Adv. Opt. Mater.* **8**, 1902092 (2020).
18. Bang, S. Y. et al. Technology progress on quantum dot light-emitting diodes for next-generation displays. *Nanoscale Horiz.* **6**, 68–77 (2021).
19. Chen, O. et al. Compact high-quality CdSe-CdS core-shell nanocrystals with narrow emission linewidths and suppressed blinking. *Nat. Mater.* **12**, 445–451 (2013).
20. Bae, W. K. et al. Controlled alloying of the core/shell interface in CdSe/CdS quantum dots for suppression of Auger recombination. *ACS Nano* **7**, 3411–3419 (2013).
21. Zhang, F. et al. Brightly luminescent and color-tunable colloidal $CH_3NH_3PbX_3$ (X = Br, I, Cl) quantum dots: potential alternatives for display technology. *ACS Nano* **9**, 4533–4542 (2015).
22. Pu, C. et al. Electrochemically-stable ligands bridge the photoluminescence-electroluminescence gap of quantum dots. *Nat. Commun.* **11**, 937 (2020).
23. Kim, T. et al. Efficient and stable blue quantum dot light-emitting diode. *Nature* **586**, 385–389 (2020).
24. Chang, Y.-T. et al. A new model for optimization of organic light-emitting device by concurrent incorporation of electrical and optical simulations. *J. Appl. Phys.* **112**, 084507 (2012).
25. Berner, D., Houili, H., Leo, W. & Zuppiroli, L. Insights into OLED functioning through coordinated experimental measurements and numerical model simulations. *Phys. Stat. Sol.* **202**, 9–36 (2005).
26. Kafafi, Z. H. et al. in *Proc. SPIE 5214, Organic Light-Emitting Materials and Devices VII* 300-309 (2004).
27. Wetzelaer, G. A. H., Kuik, M., Nicolai, H. T. & Blom, P. W. M. Trap-assisted and Langevin-type recombination in organic light-emitting diodes. *Phys. Rev. B* **83**, 165204 (2011).
28. Sirkeli, V. P., Yilmazoglu, O., Küppers, F. & Hartnagel, H. L. Effect of p-NiO and n-ZnSe interlayers on the efficiency of p-GaN/n-ZnO light-emitting diode structures. *Semicond. Sci. Technol.* **30**, 1–19 (2015).
29. Kumar, B., Campbell, S. A. & Ruden, P. P. Modeling charge transport in quantum dot light emitting devices with NiO and ZnO transport layers and Si quantum dots. *J. Appl. Phys.* **114**, 1–6 (2013).
30. Verma, U. K. & Kumar, B. Charge transport in quantum dot organic solar cells with Si quantum dots sandwiched between poly(3-hexylthiophene) (P3HT) absorber and bathocuproine (BCP) transport layers. *J. Appl. Phys.* **122**, 153104 (2017).
31. Vahabzad, F., Rostami, A., Dolatyari, M., Rostami, G. & Amiri, I. S. Solution-processed QD-LEDs in visible range: modulation bandwidth enhancement. *Phys. B* **574**, 411667 (2019).
32. Bang, S. Y. et al. Highly stable and scalable blue QD-LED via an evaporated TiO2 thin film as an electron transport layer. *Adv. Opt. Mater.* **8**, 2001172 (2020).
33. Kathirgamanathan, P., Kumaraverl, M., Bramananthan, N. & Ravichandran, S. High efficiency and highly saturated red emitting inverted quantum dot devices (QLEDs): optimisation of their efficiencies with low temperature annealed sol–gel derived ZnO as the electron transporter and a novel high mobility hole transporter and thermal annealing of the devices. *J. Mater. Chem. C.* **6**, 11622–11644 (2018).
34. Deppner, M., Römer, F. & Witzigmann, B. in *Proc. SPIE 8619, Physics and Simulation of Optoelectronic Devices XXI* 86191J (2013).
35. Puliyankot, V. & Hueting, R. J. E. One-dimensional physical model to predict the internal quantum efficiency of Si-based LEDs. *IEEE Trans. Electron Devices* **59**, 26–34 (2012).
36. Kobayashi, Y., Nishimura, T., Yamaguchi, H. & Tamai, N. Effect of surface defects on Auger recombination in colloidal CdS quantum dots. *J. Phys. Chem. Lett.* **2**, 1051–1055 (2011).
37. Qu, Y., Ji, W., Zheng, Y. & Ying, J. Y. Auger recombination and intraband absorption of two-photon-excited carriers in colloidal CdSe quantum dots. *Appl. Phys. Lett.* **90**, 133112 (2007).
38. Baranovski, S. *Charge Transport in Disordered Solids with Applications in Electronics* (Wiley, 2006).
39. Gill, W. D. Drift mobilities in amorphous charge-transfer complexes of trinitrofluorenone and poly-n-vinylcarbazole. *J. Appl. Phys.* **43**, 5033–5040 (1972).
40. Gao, X. & Yee, S. S. Hole capture cross section and enission coefficient of defect centers related to high-field-induced positive charges in SiO_2 layers. *Solid State Electron* **39**, 399–403 (1996).
41. Brotherton, S. D. & Bicknell, J. The electron capture cross section and energy level of the gold acceptor center in silicon. *J. Appl. Phys.* **49**, 667–671 (1978).
42. Engström, O., Kaniewska, M., Fu, Y., Piscator, J. & Malmkvist, M. Electron capture cross sections of InAs/GaAs quantum dots. *Appl. Phys. Lett.* **85**, 2908–2910 (2004).
43. Fu, Y., Engström, O. & Luo, Y. Emission rates for electron tunneling from InAs quantum dots to GaAs substrate. *J. Appl. Phys.* **96**, 6477–6481 (2004).
44. Wagener, M. C. et al. Hole capture and emission dynamics of type-II GaSb/GaAs quantum ring solar cells. *Sol. Energy Mater. Sol. Cells* **189**, 233–238 (2019).
45. Yang, K., East, J. R. & Haddad, G. I. Numerical modeling of abrupt heterojunctions using a thermionic-field emission boundary condition. *Solid State Electron* **36**, 321–330 (1993).
46. Kim, J. et al. A skin-like two-dimensionally pixelized full-color quantum dot photodetector. *Sci. Adv.* **5**, eaax8801 (2019).
47. Liang, C. et al. Modeling and simulation of bulk heterojunction polymer solar cells. *Sol. Energy Mater. Sol. Cells* **127**, 67–86 (2014).
48. Rosen, S., Schwartz, O. & Oron, D. Transient fluorescence of the off state in blinking CdSe/CdS/ZnS semiconductor nanocrystals is not governed by Auger recombination. *Phys. Rev. Lett.* **104**, 157404 (2010).
49. Kočka, J. & Pelant, A. F. Light emitting silicon, recent progress. *J. Non-Cryst. Solids* **198–200**, 857–862 (1996).
50. Cerdan-Pasaran, A. et al. Photovoltaic properties of multilayered quantum dot/quantum rod-sensitized TiO_2 solar cells fabricated by SILAR and electrophoresis. *Phys. Chem. Chem. Phys.* **17**, 18590–18599 (2015).
51. Xu, B. et al. Functional solid additive modified PEDOT:PSS as an anode buffer layer for enhanced photovoltaic performance and stability in polymer solar cells. *Sci. Rep.* **7**, 1–12 (2017).
52. Han, Y. J., An, K., Kang, K. T., Ju, B.-K. & Cho, K. H. Optical and electrical analysis of annealing temperature of high molecular weight hole transport layer for quantum-dot light-emitting diodes. *Sci. Rep.* **9**, 1–9 (2019).
53. Stockwell, D. et al. Comparison of electron-transfer dynamics from coumarin 343 to TiO_2, SnO_2, and ZnO nanocrystalline thin films: role of interface-bound charge-separated pairs. *J. Phys. Chem. C.* **114**, 6560–6566 (2010).
54. Wang, S. et al. Bandgap tunable $Zn_{1-x}Mg_xO$ thin films as electron transport layers for high performance quantum dot light-emitting diodes. *J. Mater. Chem. C.* **5**, 4724–4730 (2017).
55. Wang, F. et al. Achieving balanced charge injection of blue quantum dot light-emitting diodes through transport layer doping strategies. *J. Phys. Chem. Lett.* **10**, 960–965 (2019).
56. Yan, F., Parrott, E. P. J., Ung, B. S.-Y. & Pickwell-MacPherson, E. Solvent doping of PEDOT/PSS: effect on terahertz optoelectronic properties and utilization in terahertz devices. *J. Phys. Chem. C.* **119**, 6813–6818 (2015).
57. Park, Y., Choong, V., Gao, Y., Hsieh, B. R. & Tang, C. W. Work function of indium tin oxide transparent conductor measured by photoelectron spectroscopy. *Appl. Phys. Lett.* **68**, 2699–2701 (1996).
58. Vallisree, S., Thangavel, R. & Lenka, T. R. Modelling, simulation, optimization of Si/ZnO and Si/ZnMgO heterojunction solar cells. *Mater. Res. Express* **6**, 025910 (2018).
59. Kim, J. et al. ZnO nanowire-embedded Schottky diode for effective UV detection by the barrier reduction effect. *Nanotechnology* **21**, 115205 (2010).

ACKNOWLEDGEMENTS

This research was supported by the European Union under H2020 grant agreement No 685758 '1D-NEON' and by the Engineering and Physical Sciences Research Council (EPSRC) project EP/P027628/1 'Smart Flexible Quantum Dot Lighting'.

AUTHOR CONTRIBUTIONS

S.-M.J. conceived the idea and developed the simulation model. T.H.L. performed computer simulation. S.Y.B. and S.D.H. fabricated devices. D.-W.S., S.L., H.W.C. and J.-W.J. supported measurement of device performances. Y.-H.S. and X.-B.F. synthesised QD materials. S.Z. and J.Y. supported experiments. C.S. and Y.K. supported computer simulation. L.G.O. and G.A. supported data analysis. J.M.K. guided this work. S.-M.J., T.H.L. and S.Y.B. contributed equally. All the authors contributed to the preparation of the manuscript.

COMPETING INTERESTS

The authors declare no competing interests.

ADDITIONAL INFORMATION

Supplementary information The online version contains supplementary material available at https://doi.org/10.1038/s41524-021-00591-9.

Correspondence and requests for materials should be addressed to S.-M.J. or J.M.K.

Reprints and permission information is available at http://www.nature.com/reprints

Publisher's note Springer Nature remains neutral with regard to jurisdictional claims in published maps and institutional affiliations.

Open Access This article is licensed under a Creative Commons Attribution 4.0 International License, which permits use, sharing, adaptation, distribution and reproduction in any medium or format, as long as you give appropriate credit to the original author(s) and the source, provide a link to the Creative Commons license, and indicate if changes were made. The images or other third party material in this article are included in the article's Creative Commons license, unless indicated otherwise in a credit line to the material. If material is not included in the article's Creative Commons license and your intended use is not permitted by statutory regulation or exceeds the permitted use, you will need to obtain permission directly from the copyright holder. To view a copy of this license, visit http://creativecommons.org/licenses/by/4.0/.

© The Author(s) 2021